



Exploring a CNN model for earthquake magnitude estimation using HR-GNSS data

Claudia Quinteros-Cartaya^a, Jonas Köhler^{a,b}, Wei Li^a, Johannes Faber^{a,c}, Nishtha Srivastava^{a,b,*}

^a Frankfurt Institute for Advanced Studies, Germany

^b Institute of Geosciences, Goethe – University Frankfurt, Germany

^c Institute for Theoretical Physics, Goethe – University Frankfurt, Germany

ARTICLE INFO

Keywords:

Earthquake magnitude
Geodetic data
Deep learning

ABSTRACT

High-rate Global Navigation Satellite System (HR-GNSS) data can be highly useful for earthquake analysis as it provides continuous high-frequency measurements of ground motion. This data can be used to analyze diverse parameters related to the seismic source and to assess the potential of an earthquake to prompt strong motions at certain distances and even generate tsunamis. In this work, we present the first results of a deep learning model based on a convolutional neural network for earthquake magnitude estimation, using HR-GNSS displacement time series. The influence of different dataset configurations, such as station numbers, epicentral distances, signal duration, and earthquake size, were analyzed to figure out how the model can be adapted to various scenarios. We explored the potential of the model for global application and compared its performance using both synthetic and real data from different seismogenic regions. The performance of our model at this stage was satisfactory in estimating earthquake magnitude from synthetic data with $0.07 \leq \text{RMS} \leq 0.11$. Comparable results were observed in tests using synthetic data from a different region than the training data, with $\text{RMS} \leq 0.15$. Furthermore, the model was tested using real data from different regions and magnitudes, resulting in the best cases with $0.09 \leq \text{RMS} \leq 0.33$, provided that the data from a particular group of stations had similar epicentral distance constraints to those used during the model training. The robustness of the DL model can be improved to work independently from the window size of the time series and the number of stations, enabling faster estimation by the model using only near-field data. Overall, this study provides insights for the development of future DL approaches for earthquake magnitude estimation with HR-GNSS data, emphasizing the importance of proper handling and careful data selection for further model improvements.

1. Introduction

The Global Navigation Satellite System (HR-GNSS) can provide high-frequency and high-precision position measurements that facilitate the detection of ground displacements caused by earthquakes. Unlike inertial sensors, HR-GNSS instruments can record the signal of large earthquakes near the source without saturation, providing valuable information on both dynamic (far-field) and static (near-field) displacements (Bock et al., 2000; Ge et al., 2000; Kouba, 2003; Larson, 2009).

Furthermore, earthquake magnitude estimation from GNSS waveforms has been made possible through empirical relationships between the peak ground displacement and the seismic moment (Crowell et al.,

2013; Melgar et al., 2015; Goldberg et al., 2021). In the last decades, researchers have explored incorporating GNSS data to improve the accuracy of earthquake magnitude estimation compared to using seismic data alone from seismometers and accelerometers (Bock et al., 2011; Wang et al., 2013). As a result, HR-GNSS networks for earthquake monitoring and the continuous recording of data for near-real-time analysis have increased.

The 2004 Sumatra-Adaman earthquake with a magnitude of Mw 9.1 was a significant event that motivated the implementation and improvement of early warning systems in potential seismogenic regions using HR-GNSS sensors (Blewitt et al., 2006; Satake, 2014). Subsequent great earthquakes such as the Mw 8.8 Maule (2010), Mw 9.0 Tohoku (2011), and Mw 8.4 Illapel (2015), among others, have demonstrated

* Corresponding author. Frankfurt Institute for Advanced Studies, Germany.
E-mail address: srivastava@fias.uni-frankfurt.de (N. Srivastava).

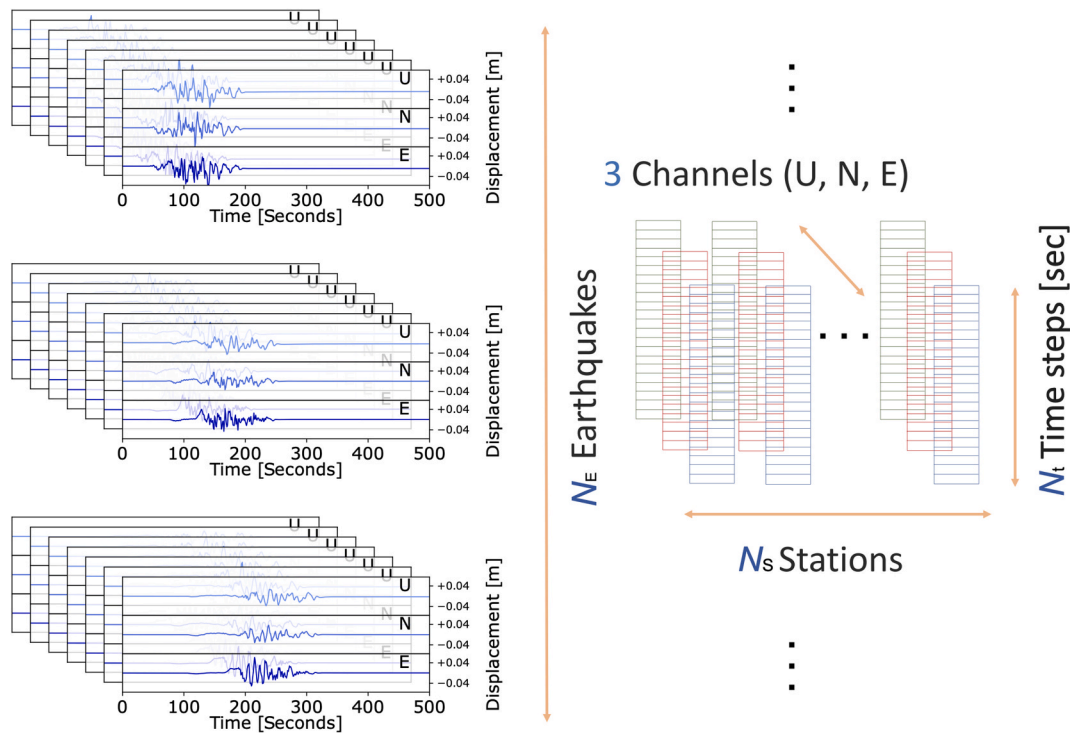


Fig. 1. The input data for the HR-GNSS displacement time series is stored in a tensor whose shape depends on the number of earthquakes (N_E), station numbers (N_s), time steps in the time series (N_t), and 3 channels (U: up, N: north, and E: east directions). The amplitudes in the time series represent displacements in meters, and the sampling rate is 1 Hz, with every time step representing 1 s in time.

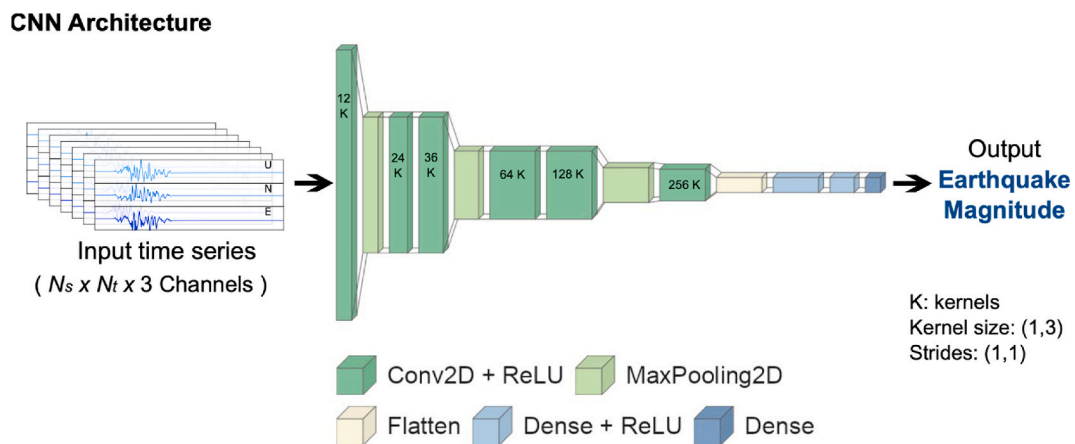


Fig. 2. Sequential Convolutional Neural Network architecture proposed in this work for earthquake magnitude estimation using displacement time series in three components (3 channels) from a specific number of HR-GNSS stations, N_s , and the number of time steps, N_t , in the time domain.

the importance of the fast and reliable assessment of seismic sources, leading to the development of diverse algorithms for HR-GNSS data analysis that enable proper early warning of earthquakes and tsunamis (e.g., Crowell et al., 2009, 2016, 2018; Allen and Ziv, 2011; Fang et al., 2014; Grapenthin et al., 2014; Minson et al., 2014; Kawamoto et al., 2016; Ruhl et al., 2017, 2019; Psimoulis et al., 2018).

Moreover, seismologists aim to develop complementary tools to outperform traditional analysis methods through deep learning (DL) approaches, which have proven to have great capacity in big data processing and feature extraction for fast and robust results. DL methods have been widely introduced to deal with various seismological tasks, such as earthquake detection, phase picking, seismic source assessment, and denoising of seismic signals (e.g., Ochoa et al., 2018; Chakraborty

et al., 2022a, 2022b; Jiao and Alavi, 2020; Kuang et al., 2021; Li et al., 2022a; Li et al., 2022b; Mousavi and Beroza, 2022; Perol et al., 2018). However, training DL algorithms with HR-GNSS data for seismic analysis is one of the most recent challenges still in development. For instance, Lin et al. (2021) worked on seismic source patterns analysis and magnitude estimation through a DL algorithm and HR-GNSS data, focusing on the seismic activity in the Chile subduction zone by using peak ground displacement time series. Also, Dittmann et al. (2022) introduced a DL algorithm for earthquake detection through velocity time series obtained from HR-GNSS by the time-differenced carrier phase. And recently, Costantino et al. (2023) presented a spatio-temporal analysis through deep learning algorithms for seismic source characterization using images from static deformation GNSS data

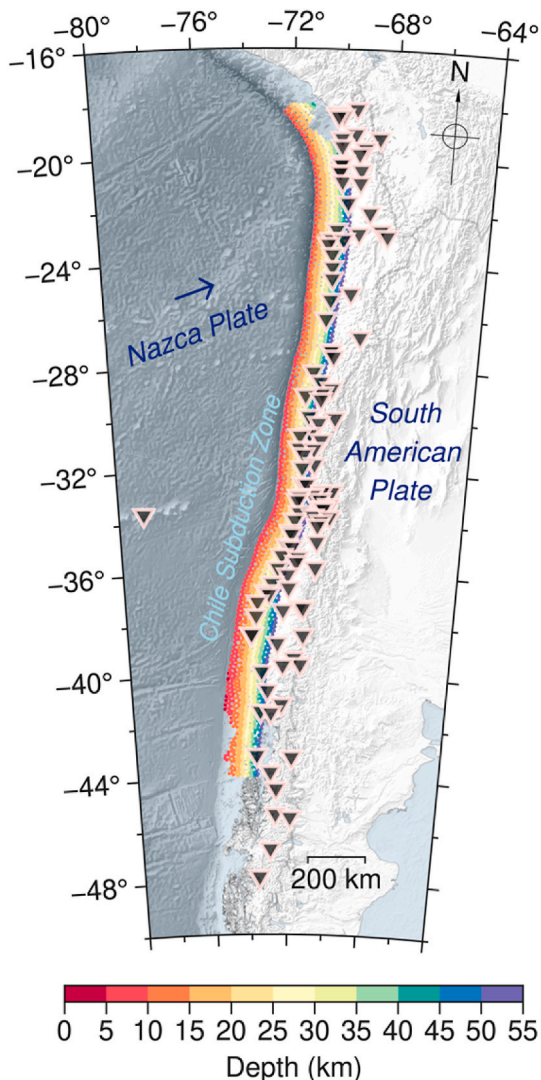


Fig. 3. Chile Subduction Zone. The synthetic data represent the displacements hypothetically recorded by the Chilean GNSS Network shown as black triangles on the map (Báez et al., 2018), corresponding to the earthquakes whose hypocenters are shown as dots in color scale by depth.

of Japan.

In this work, we present a preliminary DL model based on a convolutional neural network for the magnitude estimation from HR-GNSS dynamic data. Unlike previous algorithms, our model is trained merely on displacement time series. We tested the performance of our model using both synthetic and real data from different seismogenic regions, and thus evaluated the possibility of extending its application on a global scale. We also analyzed the influence of different dataset configurations, such as epicentral distances, signal duration, and earthquake size, to determine how the model can be adapted to different scenarios.

2. Architecture

We propose a deep learning model using a sequential Convolutional Neural Network (CNN) for a regression problem (Le Cun, 1989; Schmidhuber, 2015; Géron, 2019; Goodfellow et al., 2016). The CNN architecture consists of six 2D-convolutional layers, three max-pooling layers (Scherer et al., 2010; Zhou and Chellappa, 1988), and three fully-connected or dense layers (Le Cun et al., 1998).

The input layer for the DL model is comprised of displacement time series for each earthquake with a 1 Hz sampling rate. These time series are stored in a tensor with dimensions $N_s \times N_t \times 3$, where N_s represents the number of stations, N_t represents the number of time steps in the time series, and three channels correspond to the U, N, and E components referring to the up, north, and east directions of the sensor in each GNSS station (as shown in Fig. 1).

The architecture of our model is summarized in Fig. 2. For each convolutional layer, we used different numbers of filters with kernel size (1, 3) and stride (1, 1). No padding (“valid”) was only used in the first and the last convolutional layer, while in the intermediate layers padding was “same”. A pool size of (1, 2) was used in each max-pooling layer. Thus, we are down-sampling the data, while keeping the extraction of features in the time series separated by stations up to the dense layers.

We chose a rectified linear unit activation function (ReLU) as the transfer function to activate the output in every convolutional and dense layer (Nair and Hinton, 2010). The last tensor that results from the convolutional layers is transformed through a flattening layer to a one-dimensional vector (Krizhevsky et al., 2017) to be the input for the dense layers.

Then, the three dense layers consist of 128, 32, and 1 neuron, respectively. The weights of the kernels for the two first dense layers are initialized using a normal distribution and constrained by max-norm regularization with a maximum norm value of 3 (Géron, 2019).

Since we do not adopt any normalization for the values of the labels in the training (magnitudes), we obtain a target variable in the output layer whose value is equivalent to the earthquake moment magnitude M_w (Hanks and Kanamori, 1979).

3. Data

In general, the displacement signals of $M_w < 5$ earthquakes recorded by HR-GNSS stations are masked by noise. Small earthquakes tend to generate lower amplitude ground motions, and thus, when a shallow earthquake of around $M_w 5$ occurs, only the nearest GNSS stations located within approximately 5 km, under favorable or non-noisy site conditions, are able to well-record the ground displacement data (e.g., Mendoza et al., 2012). Also, deep earthquakes might undergo greater attenuation, resulting in weaker signals received by the GNSS stations compared to the shallower ones of the same magnitude.

For this reason, we have focused our analysis on large earthquakes, which are those better recorded by HR-GNSS stations, in most of the cases.

However, the real HR-GNSS data from large earthquakes ($M_w > 7$) available in existing datasets may not be enough to constitute a representative dataset for training a deep learning (DL) model.

Therefore, we utilized synthetic HR-GNSS signals from a previously generated database by Lin et al., 2020, which represent 36,800 rupture scenarios specifically modeled for the Chile subduction zone (Fig. 3), hypothetically recorded by the Chilean GNSS Network (Báez et al., 2018). The distribution of epicenters spans a long area of approximately 600,000 km², corresponding to earthquakes with M_w magnitude from 6.6 to 9.6, and focal depth up to 55 km.

In this initial experiment, we have used noiseless synthetic signals, since our intention is to assess the results of a simplistic model serving as the baseline for subsequent, more complex, and realistic experiments that will address this disparity by examining the impact of noise in the data.

We utilized the synthetic HR-GNSS data from the Chile region for training, validation, and testing of our DL model. Furthermore, we evaluated the performance of our model by testing it with synthetic signals of a $M_w 8.7$ Cascadia earthquake (Melgar et al., 2016) and real data (Melgar and Ruhl, 2018) from six large earthquakes from diverse regions (Fig. 4).

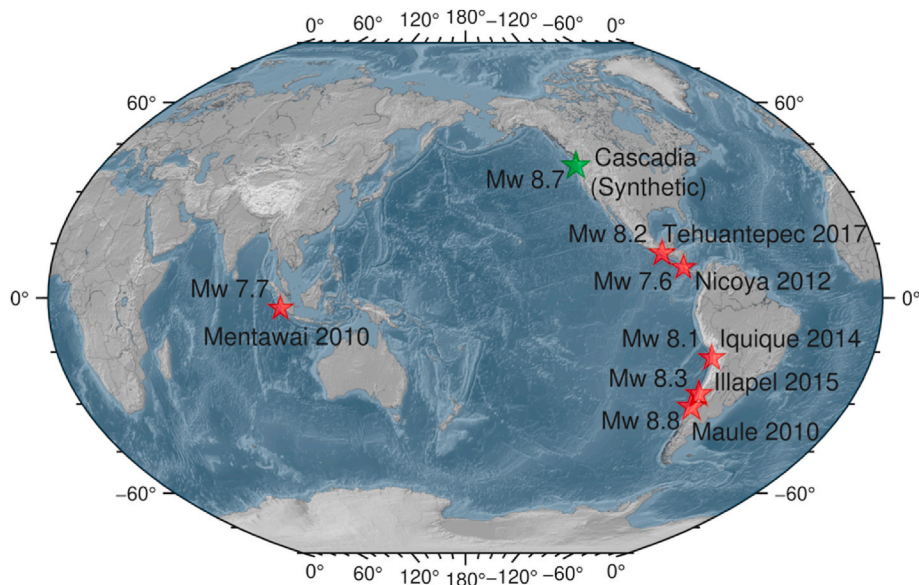


Fig. 4. Earthquakes used for testing the model. Red stars represent the epicenter of the earthquakes used with real HR-GNSS signals, and the green star is the epicenter of the Cascadia earthquake used with synthetic signals.

Table 1

Setting of the input data for the three cases. Each case corresponds to one training instance of the same architecture for the DL models, but the input data have shapes that differ between the cases.

Cases	Number of Stations per earthquake (Δ : epicentral distance)	Time series window size (seconds)	Input Data Shape
Case I	3 stations, $\Delta \leq 3^\circ$	181	$(3 \times 181 \times 3^a)$
Case II	7 stations, $\Delta \leq 3^\circ$	181	$(7 \times 181 \times 3^a)$
Case III	7 stations: from 3 to 5 stations $\Delta \leq 3^\circ$ and the rest $\Delta > 3^\circ$	501	$(7 \times 501 \times 3^a)$

^a 3 Channels: components in U, E, and N directions.

4. Training

4.1. Data preparation

Since we explore the influence of using data from different numbers of stations, epicentral distances, and time series lengths on the model performance, we prepared data sets to correspond to three cases: Case I, Case II, and Case III, which involved the training of three models with the same architecture, but using different shapes for the input data (Table 1). The initial time in the time series, $t = 0$, was referenced to the earthquake origin time. The amplitude displacements have physical units in meters, and the sampling is in the time domain, in seconds.

For Case I and Case II, we used data from three and seven stations, respectively, located within a 3° radius from the epicenter ($\Delta \leq 3^\circ$; Fig. 5a), and time series that contain 180 s after the earthquake origin time. Then, for Case III, we sought to incorporate a greater range of maximum displacements observed in the time series, particularly those in the near and mid-field (Blewitt et al., 2006). To achieve this, we utilized data from seven different stations (Fig. 5b), ensuring a balanced representation by selecting at least three and up to five stations within a radius of 3° from the epicenter. For the remaining stations farther than 3° away, we included those with epicentral distances that did not cause amplitude displacements too small to detect in the time series. The maximum distance depends on the earthquake magnitude and on how

the generation of the synthetic dataset was previously constrained (Lin et al., 2020, 2021). In this last case, Case III, every time series contains the first 500 s after the origin time of the earthquakes.

The stations were selected randomly for each case, with the caveat that we avoided having data from several stations too close to each other for a particular earthquake. We included only those cases in which at least three stations had azimuths that differed by 40° from each other. Thus, we aimed to have time series with features as different as possible, such as amplitude values, time wave arrivals, duration of the earthquake signal, and so on. Lastly, we selected a total of 34,567 earthquakes and split them into different sets: 90% for the learning process (training and validation) and 10% for testing.

4.2. Learning process

We split the synthetic dataset into a training set and a validation set, taking 90% of the earthquakes for the learning process (Fig. 6). The training set was further split into an 80/20 ratio, with 80% used for training (72% of the total earthquakes in the database) and 20% for fine-tuning hyperparameters that control the learning through the validation process (18% of the total earthquakes in the database).

The non-uniform distribution of magnitudes in the synthetic database reflects the inherent distribution found in the original dataset. Despite the imbalance in the data distribution, an aspect of the experiment is to evaluate the extent to which the model's performance might be affected by this limitation in the dataset.

Each earthquake in the training set was labeled with a target variable that corresponds to its magnitude value rounded to one decimal. The mean squared error function (MSE) was used to evaluate the losses during the training process. We optimized the model using the Adaptive Moment (ADAM) estimation method to reduce the losses (Géron, 2019; Kingma and Ba, 2015). To prevent update steps from exceeding the initial learning rate, we used a learning rate schedule with a standard decay function (decay rate = learning rate/epochs). This helped to increase the performance of the training. We set the initial learning rate to 0.01, the decay to 0.1/maximum number of epochs (see Appendix A), the maximum number of epochs to 200, and the batch size to 128. We used early stopping to reduce the possibility of overfitting, stopping the training process when the minimum validation loss was reached, with patience of 20 epochs.

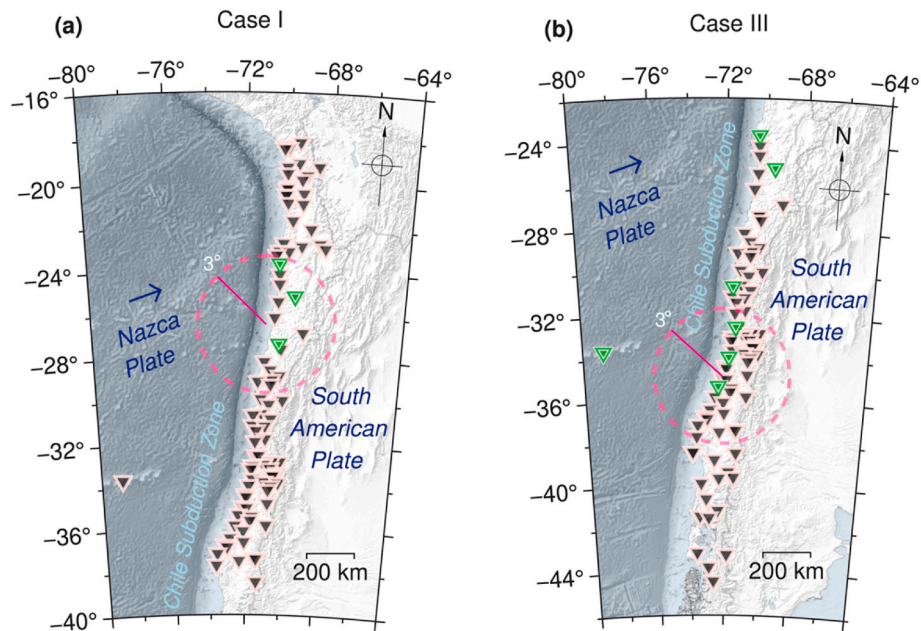


Fig. 5. Example of station distributions for the selection of data. The earthquake epicenter is in the center of the circle and the stations that were randomly chosen are shown as green triangles. In (a), three stations with epicentral distances $\Delta \leq 3^\circ$ are shown as an example of station distributions for Case I. For Case II, we could use the same example as Case I, but choose seven stations instead. In (b), a particular example of seven stations for Case III: three stations $\Delta \leq 3^\circ$, and four stations $\Delta > 3^\circ$.

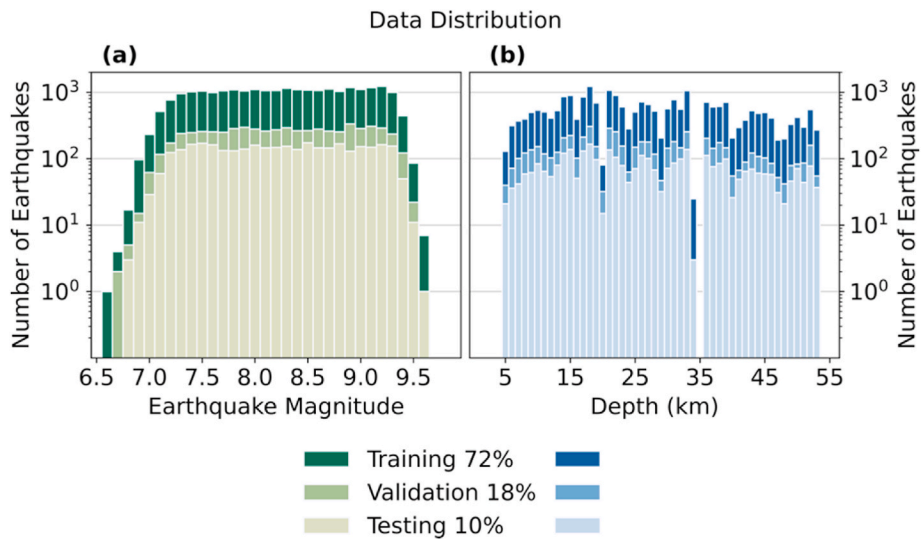


Fig. 6. Histograms of earthquake distribution in the database are shown, separated by magnitude (left) and depth (right). The dataset was split into three sets: 72% for training, 18% for validation during training, and 10% for testing. The number of earthquakes is displayed on a logarithmic scale to better visualize the smaller data groups.

5. Testing

5.1. Chile synthetic data

We evaluated the performance of the three models using 10% of the earthquakes in the database that were not used for training or validation (Fig. 6). The selection criteria for the testing set were the same as those for the training set in each case.

As shown in Fig. 7, the magnitude estimations resulted in low errors in all three cases. The lowest root mean squared error (RMS) of 0.06 was achieved in Case III, where most of the estimated magnitudes were accurate. The error distributions by magnitude are also presented in

Fig. 7d, e, and f.

In particular, for Case I and Case II, the majority of the estimated magnitudes in the range of $7.0 \leq M_w \leq 8.3$ were accurate. For Case III, the best fit was observed for almost all magnitudes, ranging from $M_w 7.0$ to 9.6. In all three cases, the errors increased with increasing magnitude. This trend was more noticeable in Case I and Case II, where the RMS values increased from $M_w 7.9$. In contrast, the RMS values slightly increased from $M_w 9.2$ in Case III.

For lower magnitudes ($M_w \leq 6.9$), the estimations were mostly overestimated in all three cases. For higher magnitudes ($M_w \geq 9.5$), the estimations were underestimated in Case I and Case II. However, due to the non-uniform distribution of earthquakes by magnitude in the testing

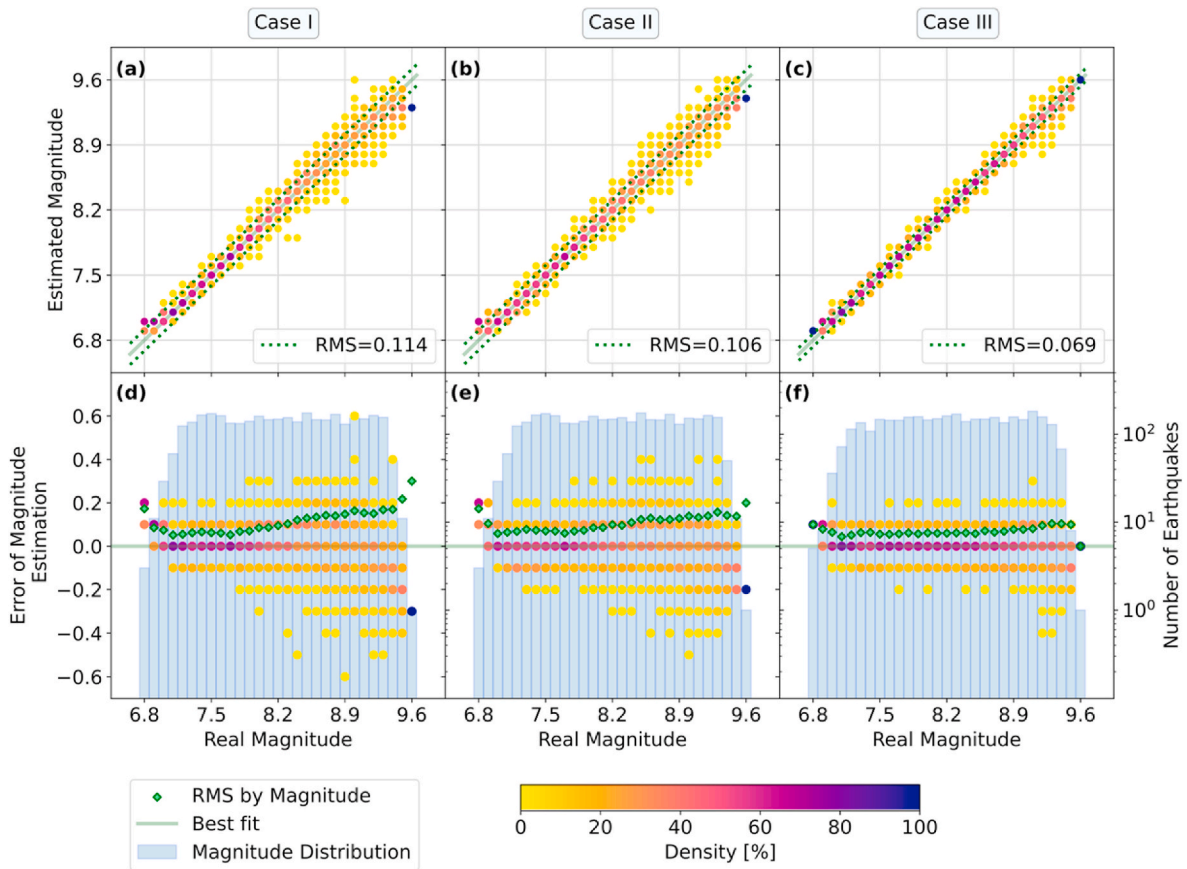


Fig. 7. Error of magnitude estimation using synthetic HR-GNSS data from Chile, for every case described in Table 1. Each circle corresponds to one bin whose color represents the percentage of tests done for each real magnitude. Plots (a), (b), and (c) are the fits of the magnitude estimations, where the RMSs are shown by the dotted lines. The results are binned on a 0.1 magnitude grid. Plots (d), (e), and (f) are the distribution of errors and RMS by each magnitude. The errors correspond to the difference between the real magnitude and the magnitude estimated by the model. The results are binned on a grid, 0.1 magnitudes \times 0.1 magnitude error. The RMS values by each magnitude are shown as green diamond symbols. The testing data distribution by magnitudes is represented through histograms in the background of the plots.

set, we had very few earthquakes with $M_w \leq 6.9$ and $M_w \geq 9.5$, resulting in a higher error for those magnitudes and an RMS value that may not be as representative as those of other magnitudes.

In the case of the highest magnitudes, the estimations may be affected by the windowing of the time series. For the largest earthquakes, 181 s in the recordings from stations nearly 3° away from the epicenter may not be long enough to contain the complete earthquake signal, resulting in an increased error in Case I and Case II. Fig. 8 shows a comparison of waveforms from earthquakes with different magnitudes and epicentral distances, in displacement time series of 181 and 501 s. For example, the synthetic waveforms of a $M_w 6.7$ earthquake with epicentral distances $\Delta \leq 3^\circ$ are complete before 150 s, whereas the waveforms of a $M_w 8.1$ earthquake, from stations $\Delta \leq 3^\circ$, just barely fit within a time window of 181 s. Furthermore, the waveforms of a $M_w 9.0$ earthquake require more than 181 s to fit the complete signal for epicentral distances larger than 1.5° .

On the other hand, the error distributions suggest that there are no features in the time series related to the earthquake depth that could have an evident influence on the estimation (Fig. 9). Nevertheless, while the error distributions did not reveal influences of depth-related features on the results, this observation does not necessarily imply the absence of such influences altogether. The analysis might have limitations in capturing depth-related features or interactions due to the specific dataset characteristics or model complexities.

5.2. Comparison using Chile and Cascadia synthetic data

To evaluate the performance of the models using synthetic data from regions with different tectonic regimes, we tested the models with two $M_w 8.7$ earthquakes: one from Chile (Lin et al., 2020) and the other from Cascadia (Melgar et al., 2016). We randomly selected a $M_w 8.7$ earthquake from the testing dataset of Chile. The data corresponded to displacement time series from 63 HR-GNSS stations for the Chile earthquake and 62 HR-GNSS stations for the Cascadia earthquake. For each earthquake, we randomly make 500 distinct combinations to group three and seven stations, depending on the case. Thus, for each case, we have an input shape (number of samples, number of stations, time steps, number of components): (500,3,181,3), (500,3,181,3), and (500,7,501,3), respectively.

In Fig. 10, the results of the models in the three cases are quite similar for both earthquakes. Although the results of the model in Case III are again the best in most estimations, with the least scattered errors and an RMS of 0.07 for Chile and 0.11 for Cascadia, in general, all three cases show a suitable performance of the model with a relatively low RMS.

There is no discernible pattern indicating whether those groups of stations farther away from the epicenter tend to have a higher error than the group with the closest stations to the epicenter. However, as we outlined in the first testing (Section 5.1), for large magnitudes, the performance of the model is better when using time series with long window sizes. Hence, we assume that the use of time series long enough in Case III could contribute to obtaining better results than in the other two cases.

Synthetic Data of Earthquakes in Chile

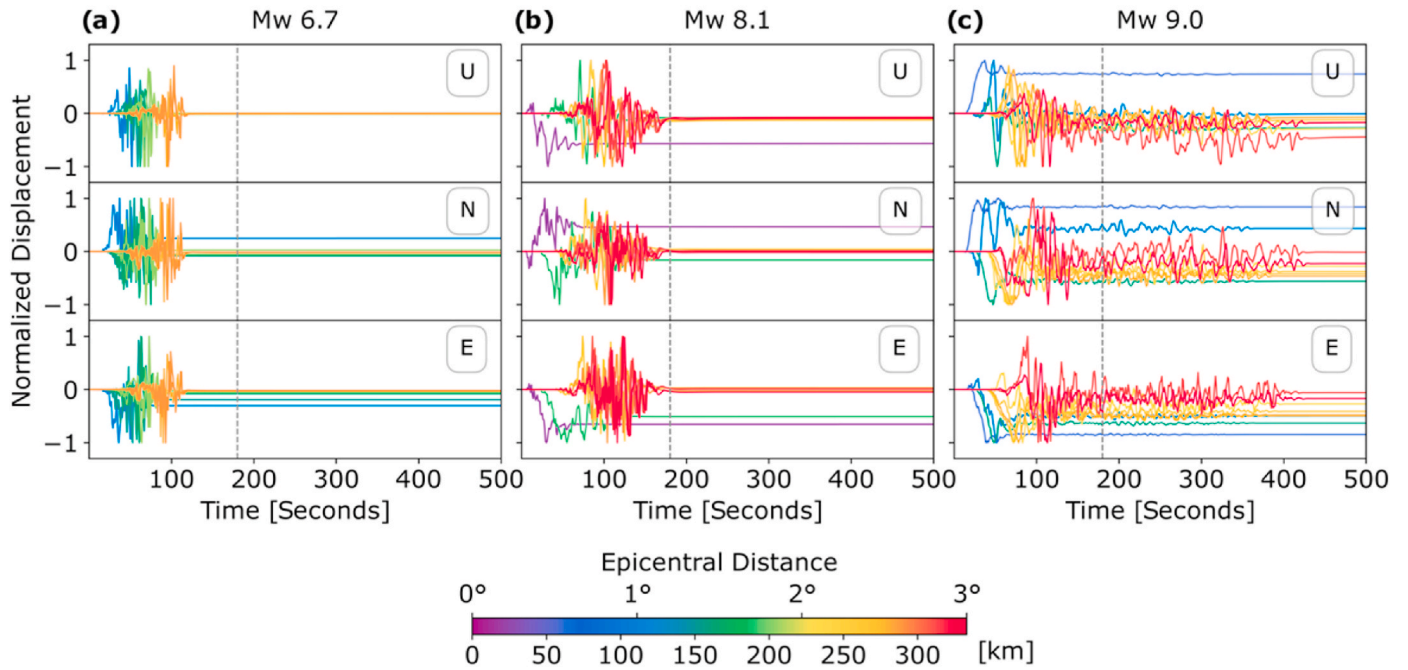


Fig. 8. Comparison of HR-GNSS synthetic data from earthquakes of magnitudes Mw 6.7, 8.1, and 9.0, in three components (U: up, N: north, and E: east directions). The initial time is referenced to the origin time of the earthquake. The amplitudes are normalized by their maximum absolute value and colors are related to the epicentral distance of stations (for distances $\Delta \leq 3^\circ$). The dashed lines refer to a window size of 181 s. Synthetic data provided by Lin et al. (2020).

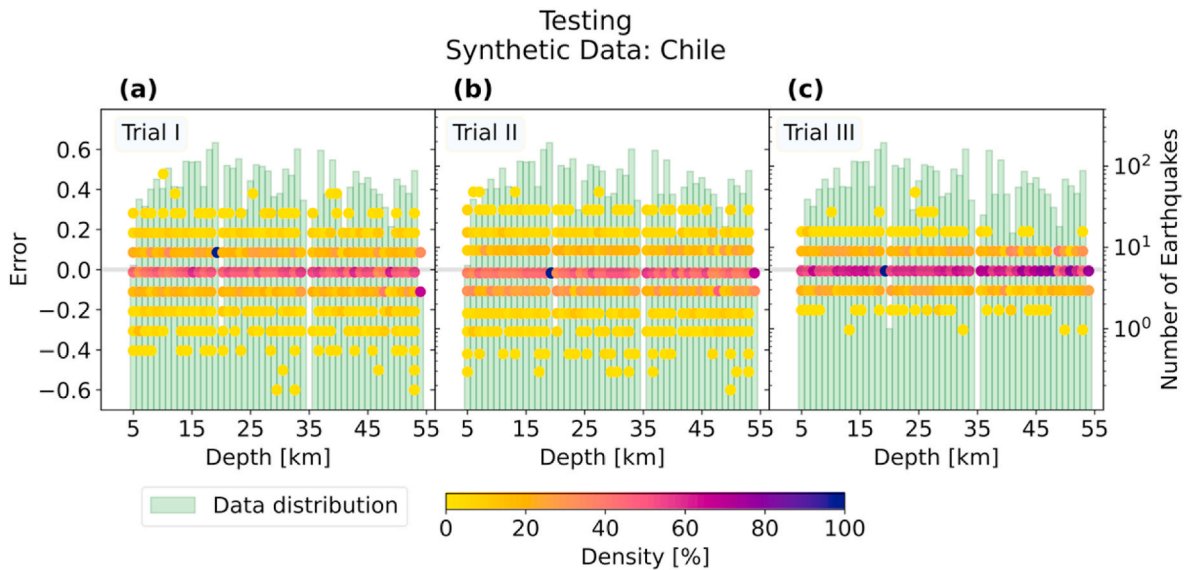


Fig. 9. Error distribution by earthquake depth. The errors correspond to the difference between the real magnitude and the magnitude estimated by the models. The results are binned on a grid, 1 km \times 0.1 magnitude error, and each circle corresponds to one bin whose color represents the percentage of tests done by each depth. The testing data distribution by depth is represented through histograms in the background of the plots. The error distributions suggest that there are no features in the time series related to the earthquake depth that could have an evident influence on the estimation.

5.3. Real earthquakes

The noise in real GNSS signals is a significant factor that could affect the accuracy of magnitude estimations, especially if the DL model used was trained with synthetic data that lacks noise. Therefore, we tested the models when faced with real HR-GNSS data from six earthquakes with different magnitudes and from different tectonic regions (Fig. 4): Maule, Iquique, and Illapel earthquakes, from Chile, and the others from

Tehuantepec (Mexico), Nicoya (Costa Rica), and Mentawai (Indonesia).

The waveforms of these earthquakes are from the database provided by Melgar and Ruhl (2018) and consist of displacement waveforms with a signal-to-noise ratio greater than 3 dB and a minimum peak amplitude of 0.04 m (Ruhl et al., 2019).

Because the number of stations in the database differs for each earthquake, we tested with different numbers of station groups for each one. We had some cases with only one group tested (Nicoya,

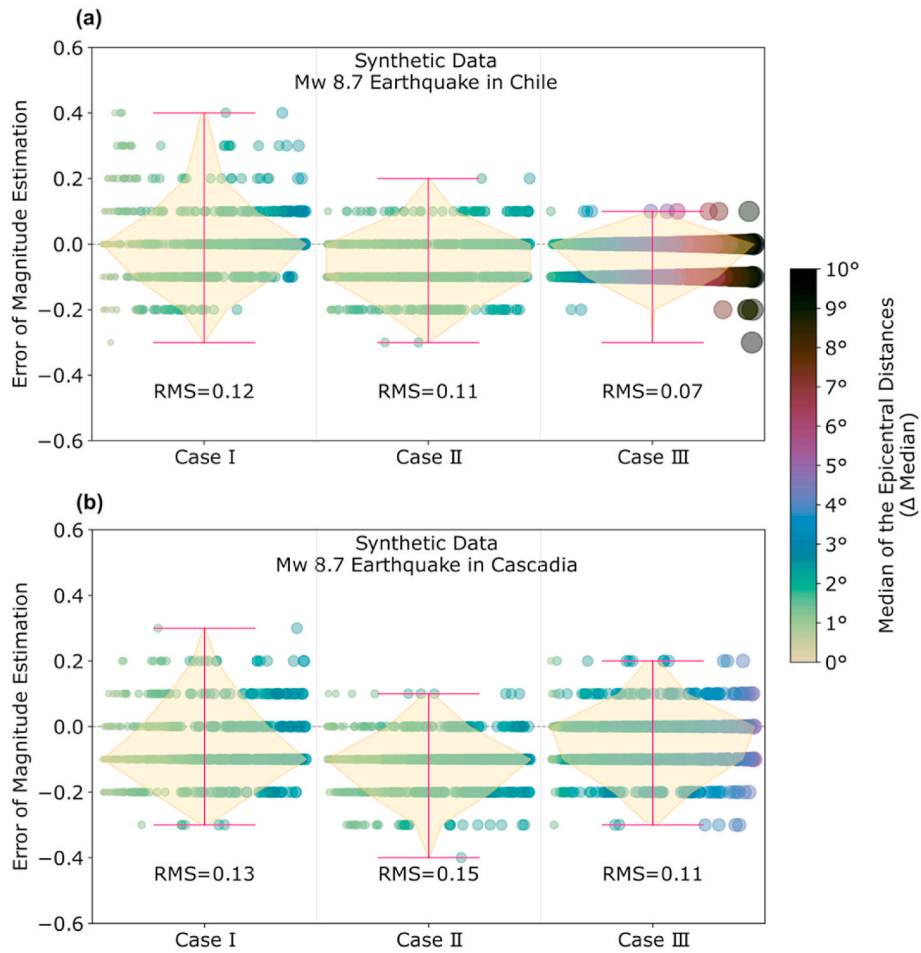


Fig. 10. Errors of magnitude estimations using synthetic data from a Mw 8.7 Cascadia and a Mw 8.7 Chile earthquake, for the DL models in the three cases (Table 1). The circles represent the magnitude error for each group of stations defined by 500 different random combinations. Both the color scale and circle sizes (sorted from left to right) depend on the median of the epicentral distances (Δ Median) of each combination of stations, in each case.

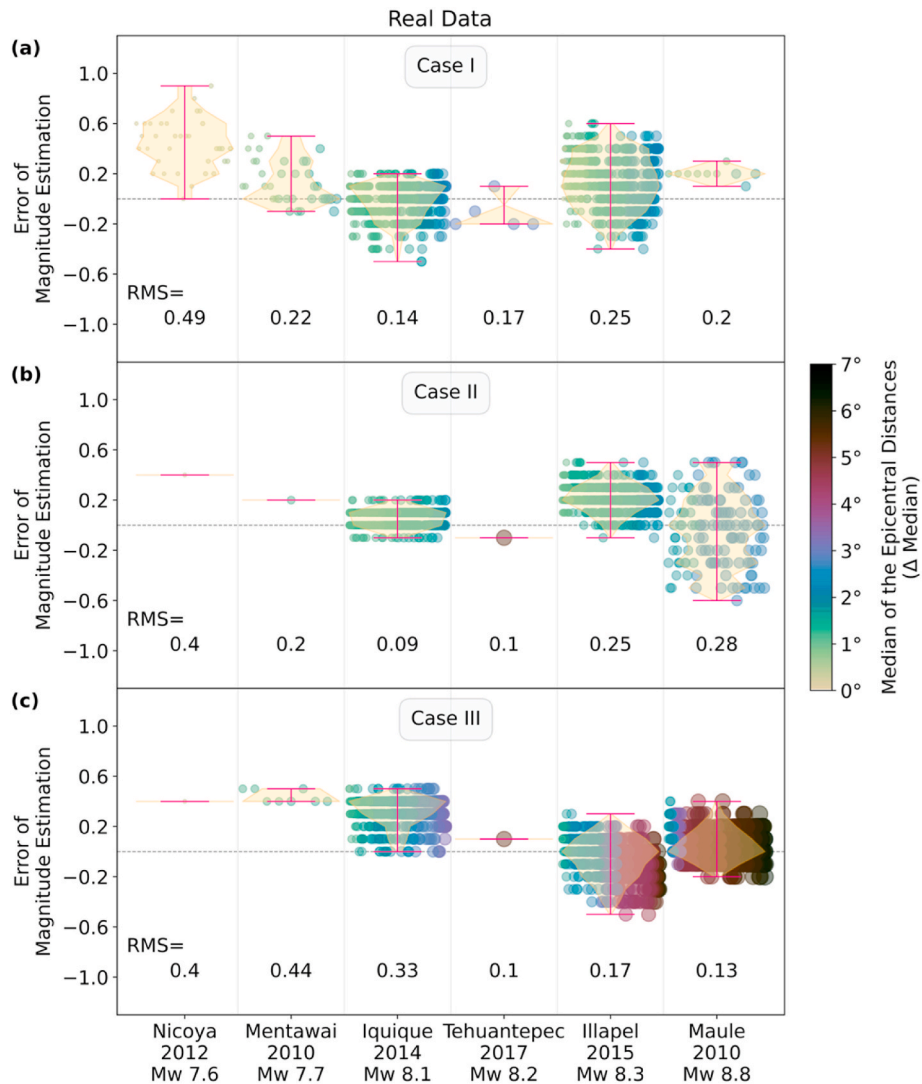


Fig. 11. Errors of magnitude estimations using real data of earthquakes from different regions and with different magnitudes. The plots correspond to the results in Case I, Case II, and Case III, from up to the bottom, respectively. The circles indicate the magnitude error for each group of stations, which were defined by different random combinations. Both the color scale and circle sizes (sorted from left to right) depend on the median of the epicentral distances (Δ Median) of each combination of stations, for each earthquake.

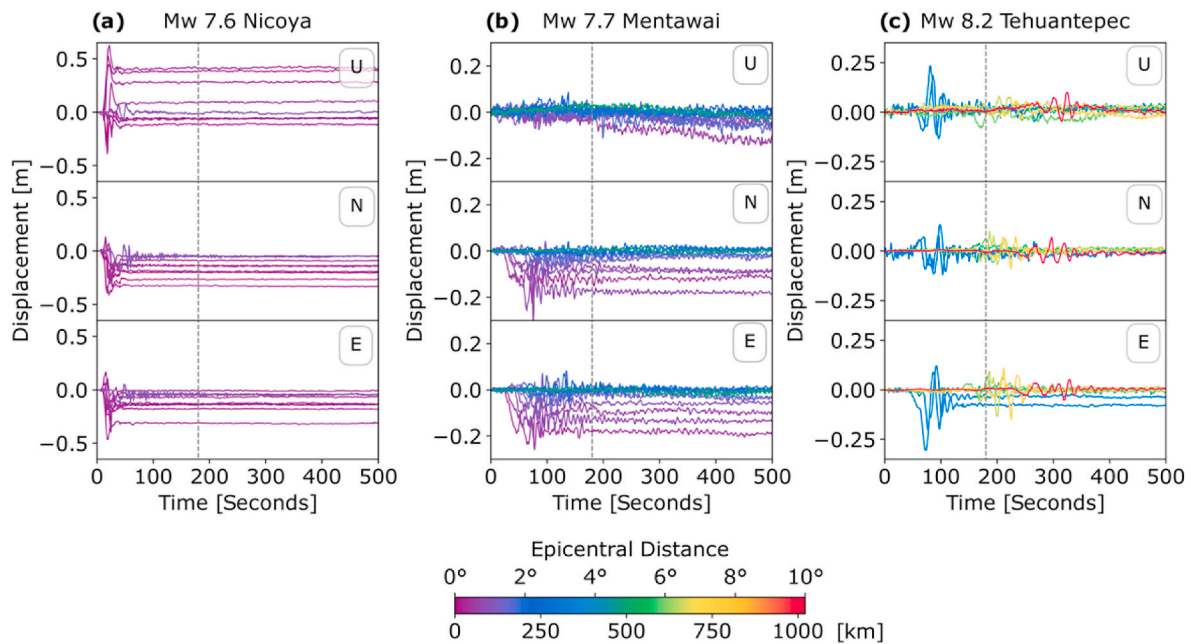


Fig. 12. Examples of HR-GNSS real data used for the model testing: Tehuantepec (Mexico), Nicoya (Costa Rica), and Mentawai (Indonesia) earthquakes. The time series are in three components (U: up, N: north, and E: east directions). The initial time is referenced to the origin time of the earthquake. The color scale is related to the epicentral distance. The dashed lines refer to a window size of 181 s.

Tehuantepec, and Mentawai), whereas for the Illapel, Maule, and Iquique earthquakes, it is possible to get thousands of possible combinations that result from hundreds of stations. Therefore, same as Section 5.2, we have limited these tests to 500 groups of stations, which is a sufficiently representative number for testing.

In Fig. 11, we show the results for every case and earthquake. The largest earthquakes: Iquique, Tehuantepec, Illapel, and Maule, had the most accurate magnitude estimations. They reached the minimum RMS values of 0.09, 0.1, 0.17, and 0.13, respectively. These results are consistent with those obtained from the testing with synthetic data. However, in some cases such as Nicoya2012 Case I, Mentawai Case I, and Maule Case II, we noticed that the errors had a more dispersed pattern. Our first assumption is that the noise content in real data could increase the error since our models are trained with ideal and clean data. We also pointed out some other observations:

1. Mw 7.6 Nicoya: the highest RMS value of 0.49 was obtained for this earthquake. All grouped stations were within an epicentral distance of less than 1° and displacements of nearly 50 cm were observed in the first 20 s (Fig. 12a). The overestimation could be because during the training rarely all stations in the same group were within such a short radius with large displacements.
2. Mw 7.7 Mentawai: the results for this earthquake are acceptable for Case I and Case II, with an RMS of 0.2. However, in Case III, the RMS of 0.44 represents a considerable error that, as for the Nicoya earthquake, could be associated with the epicentral distances of the stations used in the testing. In the test with this earthquake most of the waveforms have the largest amplitude within the first 100 s since only one station is at $\Delta > 3^\circ$ (Fig. 12b), whereas the model for this case was trained using groups with at least two stations at $\Delta > 3^\circ$, with the maximum amplitudes distributed along the 500 s of the time series (such as in Tehuantepec earthquake; Fig. 12c).
3. Mw 8.1 Iquique: as mentioned above, the magnitude for this earthquake had the best fit in Case II, with an RMS value of 0.09. However, for Case III, the RMS value was 0.33. In this case, the magnitude estimations were from groups with stations mostly at $\Delta < 3^\circ$ because

the dataset only contained three stations farther than 3.5° away (Fig. 13a).

4. Mw 8.2 Tehuantepec: seven stations were used for this earthquake and only two of them were located within a 3° radius from the epicenter (Fig. 12c). In Cases I and II, stations located more than 3° away were used in the models, which resulted in waveforms with smaller displacements than those used in the model training. Therefore, the magnitude estimations for these models were expected to be underestimated and, even so, the errors were low.
5. Mw 8.8 Maule: only five of the stations were located within a radius of 3° from the epicenter (Fig. 12c). In Case II, stations located at $\Delta > 3^\circ$ were used in the testing and hence, the insufficient time window to capture the entire signal of the earthquake at distances higher than 3° could have caused the scattered and higher errors observed in Case II.

6. Summary and conclusions

The DL architecture proposed in this work is an experimental version for earthquake magnitude estimations. It has been trained using synthetic displacement time series from groups of three and seven HR-GNSS stations, and different window sizes containing 180 s (3 min) and 500 s (just over 8 min) after the earthquake origin time. The performance of this preliminary DL model for the estimation of earthquake magnitude from synthetic data has been satisfactory.

Despite being trained with synthetic data from Chile, the model has given comparable results in tests using synthetic data from Cascadia, which represents a different tectonic region. Additionally, the results of using real data from earthquakes with different magnitudes and from different regions showed good accuracy of the estimations, provided that the data from a particular group of stations have similar epicentral distance constraints to those used during the model training. The length of the time series should also be long enough to fit most of the earthquake signals within the time window, as incomplete signals could affect the estimations.

Our experimentation across Cases I, II, and III has provided insights into the performance and limitations of our seismic magnitude

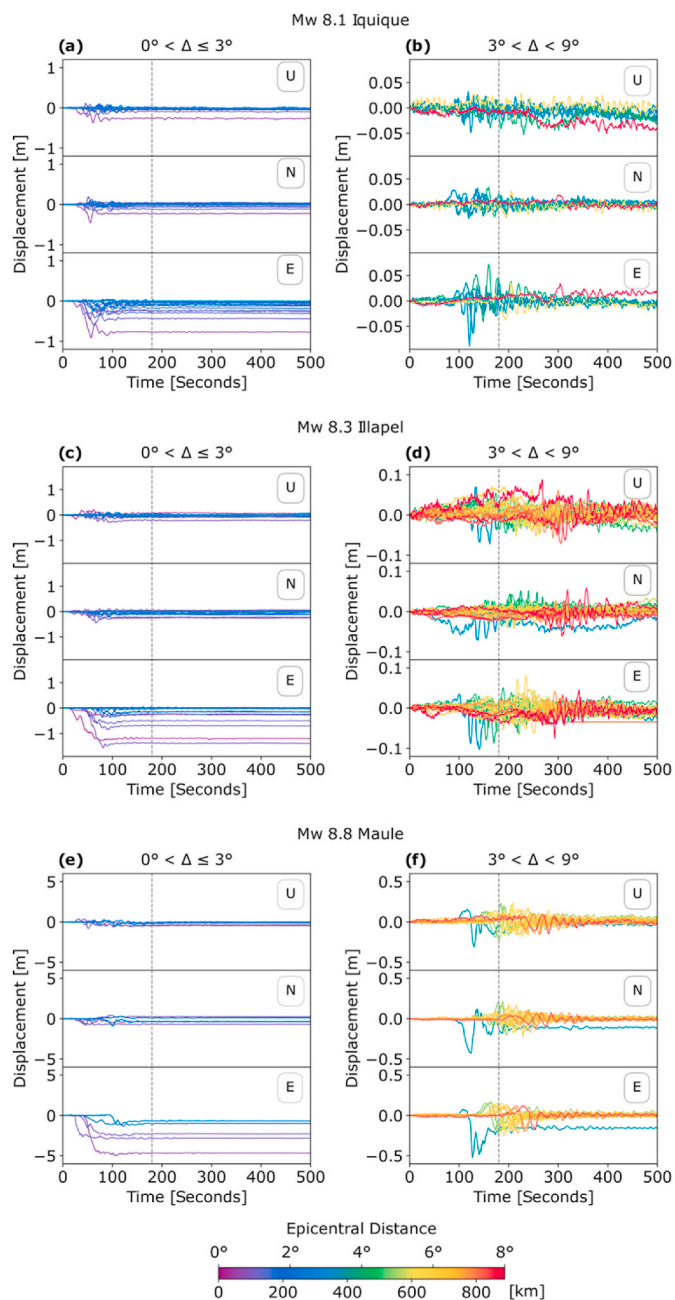


Fig. 13. Examples of HR-GNSS real data used for the model testing: Iquique, Illapel, and Maule (Chile) earthquakes. The time series are in three components (U: up, N: north, and E: east directions). The initial time is referenced to the origin time of the earthquake. On the left side, the signals are from epicentral distance $\Delta \leq 3^\circ$, and on the right, from $\Delta > 3^\circ$. Colors are related to the epicentral distance of the station. The dashed lines refer to a window size of 181 s.

estimation model. Notably, we observed distinct patterns in the accuracy of magnitude estimation across different seismic events and scenarios. Cases I and II exhibited favorable results for a majority of magnitudes within the range of 7.0–8.3, with noticeable increase in error for higher magnitudes. The shorter time windows in these cases may have contributed to challenges in capturing the complete seismic signals, particularly for larger earthquakes. On the other hand, Case III demonstrated improved performance for a broader range of magnitudes, 7.0 to 9.5, attributed to the use of longer time series.

The interesting aspect of first having been working with noiseless data lies in the ability to observe whether the model is indeed penalized

by the absence of noise in the training, and additionally, considering the epicentral distance of the record from the source. Naturally, we would expect that for longer distances, noise significantly affects the data, causing the model to have greater errors in magnitude prediction. However, the results have shown that this is not always the case and that the error does not solely depend on distance and noise, but also on the number of stations included in the analysis, the time windows length, and the magnitude.

While the DL models performed well using real data with some noise content, and regardless of the tectonic region of the earthquake, it would be advisable to evaluate their robustness by including noise in the training data.

The magnitude estimation might not be significantly affected by earthquake depth based on the analyzed time series features. However, it is important for further investigation or alternative methodologies to comprehensively explore the potential impact of depth on the model's estimation performance.

Also, addressing the challenge of dataset uniformity by magnitude or synthesizing sufficient data remains an area we intend to investigate in subsequent research endeavors.

This approach proposes a DL model designed for specific shapes of input data (number of stations and windowing), but the architecture could be improved to work independently from the window size of the time series and the number of stations. This would enable a faster estimation by the model using only near-field data from stations within a radius of less than 1° from the epicenter, which could provide reliable magnitude estimation with less than 2 min of data after the earthquake origin time.

It is worth emphasizing that the effectiveness and reliability of the models are intricately linked to how meticulously we handle and choose the data used for training. A numerical approach demands careful consideration of the data input, its quality, and relevance to ensure that the models developed through this method are robust and reflect physical realities.

The DL architecture proposed in this work is the result of a preliminary analysis. The trade-offs between time window lengths, seismic event characteristics, and noise considerations highlight areas for future exploration. As we continue to enhance our model, incorporating more realistic data scenarios and refining our training strategies, we anticipate addressing these trade-offs to improve the reliability and robustness of seismic magnitude estimations using HR-GNSS data.

Data and resources

Modeling and data processing were performed at the Frankfurt Institute for Advanced Studies, with a GPU cluster funded by BMBF for the project Seismologie und Artificielle Intelligenz (SAI). The codes are available in <https://github.com/srivastavaresearchgroup/DL-HRGNSS>. The databases used in this work were provided by <https://doi.org/10.5281/zenodo.4008690> and <https://doi.org/10.5281/zenodo.1434374>. The programming was carried out using the Python language (Pilgrim and Willison, 2009). The deep learning modeling was done using the Keras API in Python (Chollet et al., 2015). We used graphical tools from the Matplotlib and Obspy libraries in Python (Hunter, 2007; Krischer et al., 2015), as well as GMT - The Generic Mapping Tools (Wessel et al., 2019).

CRediT authorship contribution statement

Claudia Quinteros-Cartaya: Writing – review & editing, Writing – original draft, Visualization, Validation, Software, Methodology, Formal analysis, Data curation, Conceptualization. **Jonas Köhler:** Writing – review & editing, Visualization, Methodology. **Wei Li:** Writing – review & editing, Visualization, Methodology. **Johannes Faber:** Visualization, Methodology. **Nishtha Srivastava:** Conceptualization, Methodology, Writing – review & editing, Supervision, Project administration.

Declaration of competing interest

The authors declare that they have no known competing financial interests or personal relationships that could have appeared to influence the work reported in this paper.

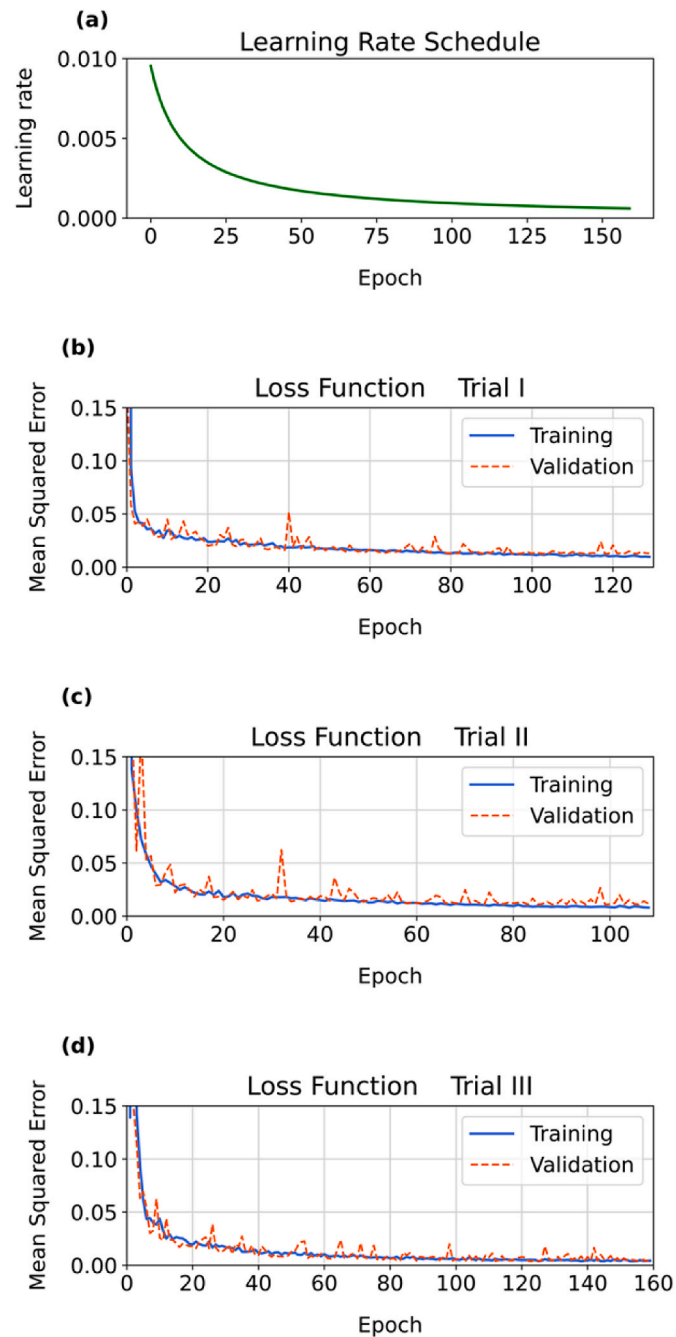
Data availability

The data and codes that support this work are openly available.

Acknowledgements

We would like to express sincere gratitude to the anonymous reviewers for their insightful comments and constructive feedback, which significantly contributed to the improvement of this manuscript. We also thank J. Alejandro González, Carlos Reinoza, and B. Crowell for the constructive comments and information about Geodesic Data analysis for seismology. This research was supported by the Federal Ministry of Education and Research of Germany (BMBF), grant SAI 01IS20059.

Appendix



Appendix A. a) Learning rate function used during the training model. b), c), and d) show the model performance during the training and validation for every case described in Table 1. The loss values for both training and validation decrease, having a very slim gap between the curves, and reaching stability to the point of low MSE values: 0.02, 0.02, and 0.01, for Case I, Case II, and Case III, respectively. Also, the number of epochs necessary to get the minimum losses with a good fit of training and validation were: 139, 108, and 134 epochs, respectively.

References

- Allen, R.M., Ziv, A., 2011. Application of real-time GPS to earthquake early warning. *Geophys. Res. Lett.* 38 (16) <https://doi.org/10.1029/2011GL047947>.
- Báez, J.C., Leyton, F., Troncoso, C., Del Campo, F., Bevis, M., Vigny, C., Moreno, M., Simons, M., Kendrick, E., Parra, H., Blume, F., 2018. The Chilean GNSS network: current status and progress toward early warning applications. *Seismol. Res. Lett.* 89 (4), 1546–1554. <https://doi.org/10.1785/0220180011>.
- Blewitt, G., Kreemer, C., Hammond, W.C., Plag, H.P., Stein, S., Okal, E., 2006. Rapid determination of earthquake magnitude using GPS for tsunami warning systems. *Geophys. Res. Lett.* 33 (11) <https://doi.org/10.1029/2006GL026145>.
- Bock, Y., Melgar, D., Crowell, B.W., 2011. Real-time strong-motion broadband displacements from collocated GPS and accelerometers. *Bull. Seismol. Soc. Am.* 101 (6), 2904–2925. <https://doi.org/10.1785/0120110007>.
- Bock, Y., Nikolaidis, R.M., De Jonge, P.J., Bevis, M., 2000. Instantaneous geodetic positioning at medium distances with the Global Positioning System. *J. Geophys. Res. Solid Earth* 105 (B12), 28223–28253. <https://doi.org/10.1029/2000jb900268>.
- Chakraborty, M., Quinteros Cartaya, C., Li, W., Faber, J., Rumpker, G., Stoecker, H., Srivastava, N., 2022a. PolarCAP – a deep learning approach for first motion polarity classification of earthquake waveforms. *Artif. Intellig. Geosci.* 3, 46–52. <https://doi.org/10.1016/j.aiig.2022.08.001>.
- Chakraborty, M., Li, W., Faber, J., Rumpker, G., Stoecker, H., Srivastava, N., 2022b. A study on the effect of input data length on a deep-learning-based magnitude classifier. *Solid Earth* 13 (11), 1721–1729. <https://doi.org/10.5194/se-13-1721-2022>.
- Chollet, F., et al., 2015. Keras. GitHub. Retrieved from <https://github.com/fchollet/keras>.
- Costantino, G., Giffard-Roisin, S., Marsan, D., Marill, L., Radiguet, M., Mura, M.D., Janex, G., Socquet, A., 2023. Seismic source characterization from GNSS data using deep learning. *J. Geophys. Res. Solid Earth* 128, e2022JB024930. <https://doi.org/10.1029/2022JB024930>.
- Crowell, B.W., Bock, Y., Squibb, M.B., 2009. Demonstration of earthquake early warning using total displacement waveforms from real-time GPS networks. *Seismol. Res. Lett.* 80 (5), 772–782. <https://doi.org/10.1785/gssrl.80.5.772>.
- Crowell, B.W., Melgar, D., Bock, Y., Haase, J.S., Geng, J., 2013. Earthquake magnitude scaling using seismogeodetic data. *Geophys. Res. Lett.* 40 (23), 6089–6094. <https://doi.org/10.1002/2013GL058391>.
- Crowell, B.W., Schmidt, D.A., Bodin, P., Vidale, J.E., Baker, B., Barrientos, S., Geng, J., 2018. G-FAST earthquake early warning potential for great earthquakes in Chile. *Seismol. Res. Lett.* 89 (2A), 542–556. <https://doi.org/10.1785/0220170180>.
- Crowell, B.W., Schmidt, D.A., Bodin, P., Vidale, J.E., Gombert, J., Hartog, J.R., Kress, V. C., Melbourne, T.I., Santillan, M., Minson, S.E., Jamison, D.G., 2016. Demonstration of the Cascadia G-FAST geodetic earthquake early warning system for the Nisqually, Washington, Earthquake. *Seismol. Res. Lett.* 87 (4), 930–943. <https://doi.org/10.1785/0220150255>.
- Dittmann, T., Liu, Y., Morton, Y., Mencin, D., 2022. Supervised machine learning of high rate GNSS velocities for earthquake strong motion signals. *J. Geophys. Res. Solid Earth* 127 (11). <https://doi.org/10.1029/2022JB024854>.
- Fang, R., Shi, C., Song, W., Wang, G., Liu, J., 2014. Determination of earthquake magnitude using GPS displacement waveforms from real-time precise point positioning. *Geophys. J. Int.* 196 (1), 461–472. <https://doi.org/10.1093/gji/ggt378>.
- Ge, L., Han, S., Rizos, C., Ishikawa, Y., Hoshida, M., Yoshida, Y., Izawa, M., Hashimoto, N., Himori, S., 2000. GPS seismometers with up to 20 Hz sampling rate. *Earth Planet Sp* 52, 881–884. <https://doi.org/10.1186/BF03352300>.
- Géron, A., 2019. *Hands-On Machine Learning with Scikit-Learn, Keras, and TensorFlow: Concepts, Tools, and Techniques to Build Intelligent Systems*, second ed. O'Reilly Media.
- Goldberg, D.E., Melgar, D., Hayes, G.P., Crowell, B.W., Sahakian, V.J., 2021. A ground-motion model for GNSS peak ground displacement. *Bull. Seismol. Soc. Am.* 111 (5), 2393–2407. <https://doi.org/10.1785/0120210042>.
- Goodfellow, I., Bengio, Y., Courville, A., 2016. *Deep Learning: Adaptive Computation and Machine Learning Series*. MIT Press. <http://www.deeplearningbook.org>.
- Grapenthin, R., Johanson, I.A., Allen, R.M., 2014. Operational real-time GPS-enhanced earthquake early warning. *J. Geophys. Res. Solid Earth* 119 (10), 7944–7965. <https://doi.org/10.1002/2014JB011400>.
- Hanks, T.C., Kanamori, H., 1979. A moment magnitude scale. *J. Geophys. Res.* 84 (B5), 2348. <https://doi.org/10.1029/JB084iB05p02348>.
- Hunter, J.D., 2007. Matplotlib: a 2D graphics environment. *Comput. Sci. Eng.* 9 (3), 90–95.
- Jiao, P., Alavi, A.H., 2020. Artificial intelligence in seismology: advent, performance and future trends. *Geosci. Front.* 11 (3), 739–744. <https://doi.org/10.1016/j.gsf.2019.10.004>.
- Kawamoto, S., Hiyama, Y., Ohta, Y., Nishimura, T., 2016. First result from the GEONET real-time analysis system (REGARD): the case of the 2016 Kumamoto earthquakes. *Earth Planets Space* 68 (1). <https://doi.org/10.1186/s40623-016-0564-4>.
- Kingma, D.P., Ba, J., 2015. Adam: a method for stochastic optimization. In: *Proceedings of the 3rd International Conference on Learning Representations (ICLR 2015)*. <http://arxiv.org/abs/1412.6980>.
- Kouba, J., 2003. Measuring seismic waves induced by large earthquakes with GPS. In: *Stud. Geophys. Geod.*, vol. 47. <http://igsbc.jpl.nasa.gov/organization/>.
- Krischer, L., Megies, T., Barsch, B., Beyreuther, M., Lecocq, T., Caudron, C., Wassermann, J., 2015. ObsPy: a bridge for seismology into the scientific Python ecosystem. *Comput. Sci. Discov.* 8 (1), 14003–14020. <https://doi.org/10.1088/1749-4699/8/1/014003>.
- Krizhevsky, A., Sutskever, I., Hinton, G.E., 2017. ImageNet classification with deep convolutional neural networks. *Commun. ACM* 60 (6), 84–90. <https://doi.org/10.1145/3065386>.
- Kuang, W., Yuan, C., Zhang, J., 2021. Real-time determination of earthquake focal mechanism via deep learning. *Nat. Commun.* 12 (1) <https://doi.org/10.1038/s41467-021-21670-x>.
- Larson, K.M., 2009. GPS seismology. *J. Geodesy* 83 (3–4), 227–233. <https://doi.org/10.1007/s00190-008-0233-x>.
- Le Cun, Y., 1989. Generalization and network design strategies. In: Pfeifer, R., Schreter, Z., Fogelman, F., Steels, L. (Eds.), *Connectionism In Perspective Elsevier*.
- Le Cun, Y., Bottou, L., Bengio, Y., Haffner, P., 1998. Gradient-based learning applied to document recognition. *Proc. IEEE* 86 (11), 2278–2324. <https://doi.org/10.1109/5.726791>.
- Li, W., Chakraborty, M., Fenner, D., Faber, J., Zhou, K., Rumpker, G., Stöcker, H., Srivastava, N., 2022a. EPick: attention-based multi-scale UNet for earthquake detection and seismic phase picking. *Front. Earth Sci.* 10 <https://doi.org/10.3389/feart.2022.953007>.
- Li, W., Chakraborty, M., Sha, Y., Zhou, K., Faber, J., Rumpker, G., Stöcker, H., Srivastava, N., 2022b. A study on small magnitude seismic phase identification using 1D deep residual neural network. *Artif. Intellig. Geosci.* 3, 115–122. <https://doi.org/10.1016/j.aiig.2022.10.002>.
- Lin, J.-T., Melgar, D., Thomas, A.M., Searcy, J., 2020. Chilean Subduction Zone Rupture Scenarios and Waveform Data (Version v2) [Data set]. Zenodo. doi:10.5281/zenodo.5015610.
- Lin, J.-T., Melgar, D., Thomas, A.M., Searcy, J., 2021. Early warning for great earthquakes from characterization of crustal deformation patterns with deep learning. *J. Geophys. Res. Solid Earth* 126 (10). <https://doi.org/10.1029/2021JB022703>.
- Melgar, D., Crowell, B.W., Geng, J., Allen, R.M., Bock, Y., Riquelme, S., Hill, E.M., Protti, M., Ganas, A., 2015. Earthquake magnitude calculation without saturation from the scaling of peak ground displacement. *Geophys. Res. Lett.* 42 (13), 5197–5205. <https://doi.org/10.1002/2015GL064278>.
- Melgar, D., LeVeque, R.J., Dreger, D.S., Allen, R.M., 2016. Kinematic rupture scenarios and synthetic displacement data: an example application to the Cascadia subduction zone. *J. Geophys. Res. Solid Earth* 121 (9), 6658–6674. <https://doi.org/10.1002/2016JB013314>.
- Melgar, D., Ruhl, C., 2018. High-rate GNSS Displacement Waveforms for Large Earthquakes Version 2.0 [Data set]. Zenodo. <https://doi.org/10.5281/zenodo.1434374>.
- Mendoza, L., Kehm, A., Koppert, A., Martín Dávila, J., Gárate, J., Becker, M., 2012. Un caso de estudio para la sismología GPS: el terremoto de Lorca. *Física Tierra* 24 (0). <https://doi.org/10.5209/rev.fite.2012.v24.40135>.
- Minson, S.E., Murray, J.R., Langbein, J.O., Gombert, J.S., 2014. Real-time inversions for finite fault slip models and rupture geometry based on high-rate GPS data. *J. Geophys. Res. Solid Earth* 119 (4), 3201–3231. <https://doi.org/10.1002/2013JB010622>.
- Mousavi, S.M., Beroza, G.C., 2022. Deep-learning seismology. *Science* 377 (6607). <https://doi.org/10.1126/science.abm4470>.
- Nair, V., Hinton, G.E., 2010. Rectified linear units improve restricted Boltzmann machines. In: Fürnkranz, J., Joachims, T. (Eds.), *ICML'10: Proceedings of the 27th International Conference on Machine Learning*. Omnipress, pp. 807–814.
- Ochoa, L.H., Niño, L.F., Vargas, C.A., 2018. Fast magnitude determination using a single seismological station record implementing machine learning techniques. *Geodesy Geodyn* 9 (1), 34–41. <https://doi.org/10.1016/j.geog.2017.03.010>.
- Perol, T., Gharbi, M., Denolle, M., 2018. Seismology convolutional neural network for earthquake detection and location. <https://www.science.org>.
- Pilgrim, M., Willison, S., 2009. *Dive into Python 3, vol. 2*. Springer.
- Psimoulis, P.A., Houlié, N., Habboub, M., Michel, C., Rothacher, M., 2018. Detection of ground motions using high-rate GPS time-series. *Geophys. J. Int.* 214 (2), 1237–1251. <https://doi.org/10.1093/gji/ggy198>.
- Ruhl, C.J., Melgar, D., Chung, A.I., Grapenthin, R., Allen, R.M., 2019. Quantifying the value of real-time geodetic constraints for earthquake early warning using a global seismic and geodetic data set. *J. Geophys. Res. Solid Earth* 124 (4), 3819–3837. <https://doi.org/10.1029/2018JB016935>.
- Ruhl, C.J., Melgar, D., Grapenthin, R., Allen, R.M., 2017. The value of real-time GNSS to earthquake early warning. *Geophys. Res. Lett.* 44 (16), 8311–8319. <https://doi.org/10.1002/2017GL074502>.
- Satake, K., 2014. Advances in earthquake and tsunami sciences and disaster risk reduction since the 2004 Indian Ocean tsunami. *Geosci. Lett.* 1, 15. <https://doi.org/10.1186/s40562-014-0015-7>.
- Scherer, D., Müller, A., Behnke, S., 2010. Evaluation of pooling operations in convolutional architectures for object recognition. In: Diamantaras, K., Duch, W.I.L. S. (Eds.), *Artificial Neural Networks – ICANN 2010*. ICANN 2010. Lecture Notes in Computer Science, pp. 92–101. https://doi.org/10.1007/978-3-642-15825-4_10.
- Schmidhuber, J., 2015. Deep learning in neural networks: an overview. *Neural Network* 61, 85–117. <https://doi.org/10.1016/j.neunet.2014.09.003>.
- Wang, R., Parolai, S., Ge, M., Jin, M., Walter, T.R., Zschau, J., 2013. The 2011 Mw 9.0 Tohoku earthquake: comparison of GPS and strong-motion data. *Bull. Seismol. Soc. Am.* 103 (2B), 1336–1347. <https://doi.org/10.1785/0120110264>.
- Wessel, P., Luis, J.F., Uieda, L., Scharroo, R., Wobbe, F., Smith, W.H.F., Tian, D., 2019. The generic mapping tools version 6. *G-cubed* 20, 5556–5564. <https://doi.org/10.1029/2019GC008515>.
- Zhou, Chellappa, 1988. Computation of optical flow using a neural network. *IEEE Int. Conf. Neural Netw.* 2, 71–78. <https://doi.org/10.1109/ICNN.1988.23914>.